SAND2014-17728J

Underlying mechanisms of increased efficiency in InGaN-based multiple quantum wells emitting at 530 - 590 nm with AlGaN interlayers

D. D. Koleske,[a,*] A. J. Fischer,[a] B. N. Bryant,[b] P. G. Kotula,[a] and J. J. Wierer, Jr.[a]

[a.] Sandia National Laboratories, Albuquerque, NM, 87185, USA

[b.] Center for High Technology Materials, Univ. of New Mexico, Albuquerque, NM, 87131, USA

Abstract

InGaN/AlGaN/GaN-based multiple quantum wells (MQWs) with AlGaN interlayers (ILs) are investigated, specifically to examine the fundamental mechanisms behind their increased radiative efficiency at wavelengths of 530 - 590 nm. The $Al_zGa_{1-z}N$ ($z \sim 0.38$) IL is ~1 - 2 nm thick, and is grown after and at the same growth temperature as the ~3 nm thick InGaN quantum well (QW). This is followed by an increase in temperature for the growth of a ~10 nm thick GaN barrier layer. The insertion of the AlGaN IL within the MQW provides various benefits. First, the AlGaN IL allows for growth of the $In_xGa_{1-x}N$ QW well below typical growth temperatures to achieve higher x (up to ~0.25). Second, annealing the IL capped QW prior to the GaN barrier growth improves the AlGaN IL smoothness as determined by atomic force microscopy, improves the InGaN/AlGaN/GaN interface quality as determined from scanning transmission electron microscope images and x-ray diffraction, and increases the radiative efficiency by reducing non-radiative defects as determined by time-resolved photoluminescence measurements. Finally, the AlGaN IL increases the spontaneous and piezoelectric polarization induced electric fields acting on the InGaN QW, providing an additional red-shift to the emission wavelength as determined by Schrodinger-Poisson modeling and fitting to the experimental data. The relative impact of these fundamental mechanisms on the radiative efficiency of MQWs with AlGaN ILs is explored along with implications to conventional longer wavelength emitters.

* ddkoles@sandia.gov

Keywords: A1 Interfaces, A1 X-ray diffraction, A3 Metalorganic vapor phase epitaxy, B2 InGaN, , B3 Light-emitting diodes, B3 Solar cells

Highlights: (need up to four highlights – single sentence describing a major finding).

1. AlGaN interlayers (IL) cap the InGaN quantum wells (QWs) enabling increased indium incorporation at lower QW growth temperatures and increased radiative efficiency for emission wavelengths of 530 - 590 nm.

2. Annealing the AlGaN IL capped InGaN QW at temperatures higher than the QW growth temperature results in a dramatic increase in photoluminescence (PL) intensity and decrease in emission linewidth.

3. Atomic force microscopy, time resolved PL, x-ray diffraction, and scanning transmission electron microscopy show improved heterointerfaces of the InGaN/AlGaN/GaN multiple quantum well and fewer non-radiative recombination centers.

4. The AlGaN IL increases the polarization induced electric fields within the InGaN QW providing a significant red-shift the emission wavelength.

Statement of Original Work:

This paper describes the fundamental mechanisms behind the increased PL intensity and smoother interfaces for InGaN QW capped with an AlGaN interlayer. This manuscript is the original work of the authors' and has not been published nor has it been submitted simultaneously elsewhere. All authors have checked the manuscript and have agreed to the submission.

1. Introduction

The efficiencies of InGaN based light-emitting diodes (LEDs) and laser diodes (LDs) have developed rapidly in the last decade, resulting in commercial products such as retrofit LED light bulbs and LD sources for high density optical drives [1-4]. These high efficiencies are achieved at violet-blue wavelengths (400-465nm) with $In_xGa_{1-x}N$ quantum wells (QWs) that contain modest indium concentrations (x~0.05 - 0.15). Increasing the indium concentration beyond x~0.15 can result in green to red wavelengths, but at the expense of efficiency [5]. This decrease in LED efficiency for $x > 0.15$ in conjunction with an opposing decrease in the efficiency of AlInGaP LEDs from red to yellow wavelengths has been called the "green gap" [2; 6]. For InGaN LEDs within the green gap incremental efficiency improvements continue, yet there are few commercial LED or LD products emitting at these wavelengths. In addition, other InGaN optoelectronic devices such as solar cells are also limited. Ideally, InGaN should span nearly the entire solar spectrum [7], but because of the poor material quality at longer wavelengths, InGaN-based solar cells exhibit lower power conversion efficiencies [8; 9] when compared to more conventional solar cell materials.

Various mechanisms have been proposed to explain the decreased efficiency of InGaN alloys as the indium concentration increases. These include: 1) lattice mismatch strain of InGaN layers grown on GaN which manifests itself in the formation of non-radiative defects [10] and surface roughening [11; 12]; 2) the low growth temperatures required to incorporate sufficient indium results in the incorporation of impurities[13; 14], point defects [15], and V-type defects[16], all of which have been proposed to act as non-radiative recombination centers [17; 18]; and 3) large piezoelectric-polarization-induced electric fields which separate the QW electron and hole wavefunctions and decrease their overlap, resulting in decreasing their spontaneous recombination rate [19]. Less probable as an explanation is the miscibility gap in the InGaN crystal phase resulting in poor crystalline material as proposed by Ho and Stringfellow [20],

since green emitters within this miscibility gap have been shown to contain uniform, random InGaN alloys with relative smooth interfaces [21; 22].

These various mechanisms are of particular relevance to this paper, as improvements in LED intensity at longer wavelengths (560 to 629 nm) from InGaN QWs grown by metal-organic vapor phase epitaxy (MOVPE) have been recently reported in ground-breaking work at Toshiba [23-26]. For this improvement the Toshiba group used AlGaN interlayers (ILs) to cap the InGaN QWs to achieve an external quantum efficiency (EQE) of ~20% (@ 20 mA) for yellow (560 nm) LEDs [25] and ~3% (@ 20 mA) for red (629 nm) LEDs [26]. For the yellow emitting LEDs, this efficiency is approximately two times greater than that of the standard planar InGaN/GaN MQW LEDs [25]. In addition to the Toshiba work, prior work by Lin *et al.* showed that internal quantum efficiencies of green wavelength lasers on semipolar substrates could be improved using AlGaN barriers compared to GaN or InGaN barriers [27]. The Toshiba group proposed possible explanations for the improved efficiency with AlGaN ILs, including improved heterointerfaces, higher crystalline quality, and a polarization field shift of electron and hole wavefunctions. However the exact contribution and validity of each of these explanations is uncertain.

In this paper, MOVPE grown InGaN-based MQWs capped with similar AlGaN ILs are investigated, specifically to explore and comment on the relative importance of the mechanisms (namely 1-3 listed above) underlying the increased efficiency at green-gap wavelengths (530-590 nm). Section 2 captures the essential experimental details including growth and characterization. Section 3 describes the theory used to model how the polarization induced fields influence the QW emission wavelengths and intensities. The experimental results in Section 4 show how the AlGaN IL increases indium incorporation, improves the heterointerface smoothness, reduces non-radiative defects upon annealing, and red-shifts the QWs emitting wavelength as a result of the increased strength of the polarization induced electric fields. Section 5 discusses how the AlGaN IL might allow for increased incorporation of indium above the coherency strain upper

limit (x > 0.20) commonly needed to achieve green wavelength QWs on c-plane GaN, how annealing drives non-radiative defect reduction and partial strain relaxation in AlGaN/InGaN layers, and how much the enhanced polarization fields can red-shift the photoluminescence (PL) emission wavelength. Finally, in Section 6 the salient points in this paper are summarized, along with speculation on the potential for AlGaN ILs to further increase the efficiency of long wavelength LEDs and on the implications of this work on InGaN films in general.

2. Experimental Details

The QW structures were grown in a Veeco D125 short-jar MOVPE system. Growth temperatures were controlled using mid-IR pyrometers with direct optical access to the growth surface and confirmed with an emissivity-corrected UV (~405nm) pyrometer [28]. GaN templates were grown on c-plane sapphire at 500 torr (66.7 kPa) and 1050 ºC using trimethylgallium (TMGa) and NH_3 in H_2 and N_2 using the two-step approach of Nakamura [29]. The first ~2 μm thick GaN templates were undoped followed by ~2 μm Si doped GaN using SiH_4 to a carrier concentration of $5x10^{18}$ cm^{-3} as measured by Hall Effect. The GaN templates have total threading-dislocation densities averaging ~$8x10^8$ cm^{-2} as determined by x-ray diffraction analysis [30]. The QW active regions were grown at 300 torr (40.0 kPa) using 15 standard liters per minute (SLM) of NH_3 and 10 SLM of N_2 [31]. Prior to the growth of the QW structures, an $In_yGa_{1-y}N$ underlayer (UL) (y = 0.025-0.035) was grown at 850 ºC for 30 min to a thickness of ~ 150-170 nm using 97 μmole/min trimethylindium (TMIn) and 43 μmole/min of TMGa. The InGaN UL was capped with 8 nm Si-doped GaN barrier layer, prior to the growth of the first QW.

The five period InGaN/AlGaN/GaN MQWs were grown in the following way. The $In_xGa_{1-x}N$ QWs and $Al_zGa_{1-z}N$ interlayers (IL) were grown at fixed growth temperatures ranging from 700 to 740 °C, while the GaN barrier layers were grown from 800 to 900 °C. The sequence consisted of the $In_xGa_{1-x}N$ QW growth using TMIn and TMGa, followed by turning off the TMIn and

turning on the TMAl for the growth of the $Al_zGa_{1-z}N$ IL, after which both the TMGa and TMAl were turned off. The $Al_zGa_{1-z}N$ IL has $z = 0.38$, and a thickness that varies from 1.0 - 1.9 nm as measured by x-ray diffraction (XRD) which is described below. After the IL growth, the temperature was increased to the GaN barrier growth temperature and TMGa was turned on. After the Si-doped GaN barrier growth, the temperature was reduced for the next QW and IL growth sequence. For the final sequence, the InGaN/AlGaN/GaN MQW stack was capped with a GaN barrier. The precursor flows were 97 μmole/min TMIn and 6.9-27.8 μmole/min of TMGa for the QW, 18.4 μmole/min TMAl and 13.9 μmole/min of TMGa for the IL, and 13.9 μmole/min of TMGa for the GaN barrier layer.

Following growth, XRD analysis was performed using ω/2θ scans about the (0002) reflection of GaN using a Panalytical X'Pert MRD Pro X-ray diffractometer. The XRD scans were fit using X'Pert Epitaxy 4.0 to deduce the indium and aluminum concentrations and layer thicknesses for each structure under the assumption of full coherency strain of the InGaN and AlGaN layers to the underlying GaN lattice. In addition, all MQW fits assume abrupt interfaces with discrete changes in alloy concentrations and no compositional grading of the interfaces. While this assumption is valid for fits near the GaN main diffraction peak it is less valid when fitting higher order superlattice peaks as described by Lee *et al.* [32]. The IL aluminum concentration and thickness were determined separately using XRD analysis of the same MQW growth run without TMIn flowing during the MQW growth. Usually, aluminum and indium concentrations can be obtained to within 1% and thicknesses to ~ 0.1 nm. Scanning transmission electron microscopy (STEM) images were acquired with a FEI Company Titan G2 80-200 operated at 200kV and equipped with a spherical aberration corrector on the probe forming optics and four silicon-drift (SDD) energy-dispersive X-ray detectors (EDX). The X-ray detectors were used to verify the composition of the layers while high-resolution high-angle annular dark-field (HAADF) STEM images were used to verify layer thickness and interface quality. Samples for STEM were prepared by focused ion beam (FIB) milling with a FEI

Company Helios-600 dual-beam FIB-scanning electron microscope with the final thinning using 2 kV Ga^+.

Optical emission from these structures was measured by room temperature PL using a Nanometrics RPM2000 PL mapper equipped with a continuous wave, 5mW, 325 nm HeCd laser. Time-resolved PL (TRPL) data was measured separately using a Ti:Sapphire laser operating at 407 nm with a pulse width of 2 ps. PL decay times were measured using a Hamamatsu streak camera with an attached 0.5 m spectrometer resulting in lifetime data that were measured from a 20 nm spectral band at the center of the PL peak. The overall system temporal resolution was ~ 25 ps.

3. Theory

The influence of the spontaneous and piezoelectric polarization on the QW emission was calculated using the nextnano3 Schrodinger-Poisson solver software [33] for comparison with the experimental results. The simulation uses band structure parameters and effective masses for the electrons and holes from Vurgaftman and coworkers [34]. These simulations provide the energy band diagram, emission wavelengths, and the overlap of electron and hole wavefunctions within the QWs.

In these experiments, the introduction of the AlGaN IL on top of the InGaN QW changes the polarization induced fields within the QW and the resulting shape and position of the electron and hole wavefunctions. This in turn changes the spatial overlap of the wavefunctions and hence the radiative recombination rate. This expression for the radiative recombination rate can be simplified to make comparisons of MQWs where only the AlGaN IL thickness and indium composition of the InGaN QW are changed. Most variables that determine the recombination rate, such as the carrier occupation probability and carrier mass, change only slightly for this comparison and therefore are assumed constant. With this assumption, changes in the radiative

recombination rate (R_{rad}) are due to changes in the overlap of the electron and hole wavefunctions, which can be simplified to,

$$R_{rad} \propto |I|^2, \tag{1}$$

where $|I|^2$ is the square of the electron and hole wavefunction overlap integral within the QW. Here only the ground states in the QW are considered.

The IL thickness or indium composition of the InGaN QW may also affect the number of non-radiative recombination centers in the MQW. Therefore it is necessary to determine not only R_{rad}, but the radiative efficiency (η_{rad}) which includes the radiative and non-radiative recombination rate (R_{nr}), and can be expressed as:

$$\eta_{rad} = {R_{rad}}/{(R_{nr} + R_{rad})}. \tag{2}$$

In this equation changes in R_{rad} are known from Eqn. 1 using the Schrodinger-Poisson solver while R_{nr} is unknown and is determined by comparing results from the simulation to the experimental data. R_{nr} could include both Shockley-Read-Hall (SRH) and Auger recombination, but at the low PL pump intensities and resulting carrier densities used in this work SRH dominates and Auger can be ignored.

To compare the simulated η_{rad} to experimental data it is assumed that changes in the PL intensity of the MQWs (P_{out}) are approximately equal to changes in η_{rad}. This approximation assumes the percentage of absorption (A) of the input pump power (P_{in}) and light extraction efficiency (η_{ext}) of the emitted light is identical for every sample. The radiative efficiency excited by PL can be expressed as:

$$\eta_{rad} = {P_{out}}/{(P_{in} \cdot A \cdot \eta_{ext})} \tag{3}$$

If all samples are measured with the same input power, the dominator in Eqn. 3 is the same for all samples (constant). Therefore when comparing samples, changes in the experimental P_{out} are proportional to changes in experimental η_{rad}, offset by a constant factor equal to $P_{in} \cdot A \cdot \eta_{ext}$.

4. Results

4.1 Increase in emission wavelength with indium composition with and without ILs.

PL scans are shown in Fig. 1(a) along with microscope images of the surface under PL excitation for IL-MQWs with three different QW growth temperatures. For this set of growths the $In_xGa_{1-x}N$ QWs were capped with a 1.5 nm thick $Al_zGa_{1-z}N$ IL with z = 0.38. After the QW and IL growth the layers were heated to 800 ºC followed by the growth of the GaN barrier. As the QW growth temperature decreases the emission wavelength red-shifts to the difficult to achieve green-gap wavelength region. In Fig. 1(b) the PL intensities for MQWs with AlGaN ILs (left axis, red circles) and without ILs (left axis, blue squares) are plotted vs. the resultant PL wavelength. For this data, the MQW growth temperature is varied to change the emission wavelength. Note that MQWs without AlGaN ILs (blue squares) decrease in PL intensity as the wavelength increases more rapidly compared to MQWs with AlGaN ILs. For example, near ~ 545 nm MQWs with ILs are ~10x brighter than MQWs without the ILs, similar to previous reports [35]. Also shown in Fig. 1(b) is the emission full width at half maximum (FWHM) for the MQWs (right axis, green diamonds) with AlGaN ILs. As the PL wavelength increases the emission FWHM gradually increases from ~35 nm at λ = 501 nm to 73 nm at λ = 586 nm. A larger increase in the emission FWHM vs. emission wavelength occurs for MQWs without ILs (not plotted) with a FWHM of 32 nm at λ= 515 nm up to FWHM of 77 nm at 545 nm. This figure shows that yellow wavelength emission is enabled using the AlGaN ILs [23-25]. In the rest of this section, the origin of this improvement in PL emission compared to conventional InGaN/GaN MQWs is explored.

4.2 Heterointerface crystal quality with and without ILs.

MQWs with and without AlGaN ILs are compared using STEM as shown in Fig. 2. The HAADF STEM images are collected using low electron current (<75 pA) to avoid damage of the InGaN QWs during imaging [36]. In Fig. 2(a), an annular dark-field STEM image measured at the [11-20] zone is shown of a conventional, five period InGaN/GaN QW sandwiched between GaN barrier layers. The inset in Fig. 2(a) shows an atomic scale magnified section of one of the QWs. For this MQW, the $In_xGa_{1-x}N$ QW is grown at a temperature of 730 ºC resulting in $x \sim 0.20$ and capped with ~1 nm of GaN prior to heating the sample to 800 ºC to complete the GaN barrier growth. The inset STEM image in Fig. 2(a) shows a more abrupt atomic contrast on the bottom of the QW compared to the top of the QW, which shows a more gradual change (3-6 atomic planes) in the indium concentration both vertically and laterally. From EDX measurements (not shown), the indium tails into the GaN barrier layer over a distance of 1.5 to 2.0 nm. This increased atomic-scale roughness in this top layer interface is likely the result of multiple step height formation [11] and/or increased indium compositional grading [32].

In contrast to this rougher top QW interface, AlGaN IL capping of the InGaN QW shows improved interface abruptness as shown in Fig. 2(b). This STEM image measured at the [10-10] zone shows the InGaN QW (light contrast) capped by the AlGaN IL (dark contrast). As shown in Fig. 2(b), the extent of atomic mixing between the InGaN QW and AlGaN IL visually occurs over only 1 - 2 atomic planes or ~1 nm as measured from the EDX elemental compositions (not shown). These results indicate smoother and more abrupt heterointerfaces for the InGaN/AlGaN(IL)/GaN sample which, as discussed later, has consequences for both the structural and optical properties of these IL capped samples.

Several examples of ω/2θ x-ray diffraction (XRD) scans from MQWs with and without the AlGaN IL layers are shown in Fig. 3. Figs. 3(a) and 3(b) show XRD ω/2θ scans of InGaN/GaN MQWs with no AlGaN IL with the XRD scan shown in Fig. 3(b) being the same sample shown

in Fig. 2(a). The two differences between these two samples are the QW growth temperature (725 ºC for Fig. 3(a) and 730 ºC for Fig. 3(b)) and the QW growth rate which is 4 times faster for Fig. 3(b) compared to Fig. 3(a). Both wafers have a yellowish appearance with a slight hint of gray for the sample shown in Fig. 3(a), suggesting possible indium or gallium metal inclusions although no evidence of metal was observed in the XRD scan [37]. For both samples in Figs. 3(a) and 3(b), the indium fraction is x~0.20 as determined from dynamic diffraction analysis. The PL wavelength for the sample shown in Fig. 3(a) is 520 nm and for the sample shown in Fig. 3(b) is 526 nm. The presence of weak superlattice peaks for $\omega \leq 15°$, suggests some degree of top layer interface abruptness. [32]. For InGaN QW growth temperatures less than 725 °C, further graying of the structure is observed along with decreased MQW superlattice peak intensity, increased peak width as ω decreases, and the absence of peaks for angles < 15°. Each of these observations from the XRD scan suggest a loss of the MQW interface fidelity due to increased step structure [11] and/or compositional grading [32].

The influence of adding the AlGaN IL to cap the InGaN QW prior to growing the GaN barrier is shown in Figs. 3(c) and 3(d), where the GaN barriers are grown at 800 and 850 °C, respectively. The XRD scan shown in Fig. 3(d) is the same sample used in the STEM image in Fig. 2(b). For these two samples, the QW was grown at 700 °C, well below typical QW growth temperatures (~730 °C) required to prevent gray appearing MQW films. The XRD scan for the 800 °C GaN barrier sample shown in Fig. 3(c) has increasing XRD peakwidths from 17° to 15° and a near absence of superlattice peaks for angles < 15°, suggesting a similar degree of disorder to the scans shown in Figs. 3(a)-(b). For this film, the indium concentration and QW thickness were x = 0.24 and 3.3 nm thick, resulting in a PL wavelength of 574 nm with a FWHM of 74 nm. In contrast, the sample with 850 °C GaN barriers shown in Fig. 3(d) results in sharper and more intense superlattice peaks out to an angle of 13.8°. Observing these higher order superlattice peaks implies smoother and more abrupt InGaN/AlGaN heterointerfaces and less indium segregation into the AlGaN layers, both of which are observed in the STEM cross-section shown

in Fig. 2(b). The InGaN QWs shown in Fig. 3(d) have an indium composition of $x = 0.235$ and are 3.0 nm thick, resulting in a PL emission wavelength of 558 nm and a FWHM of 42 nm. The reduced indium in the Fig 3(d) sample compared to the Fig 3(c) sample suggests a slight loss of indium from the QW must occur during annealing and stronger evidence for this loss of indium will be provided in the next section. In addition, the PL wavelengths measured on both samples is consistent with increased indium in the QW and the increased polarization field influence on the QWs.

4.3 Influence of annealing on QW interface smoothness and photoluminescence intensity

To investigate the fundamental mechanisms behind the improved heterointerfaces in the IL MQWs, a single QW growth cycle was studied with "snapshots", taken by temperature quenching just after the various steps during the growth sequence. Results of the PL intensity (left axis) and FWHM (right axis) for the growth sequence are shown in Fig. 4. The inset shows the overall structure (bottom to top) which consists of a GaN barrier structure grown at 850 °C (light blue) on top of an InGaN UL (not shown), a InGaN QW grown at 700 °C (purple), a AlGaN IL grown at 700 °C (gray), and a thin GaN cap layer at 850 °C (light blue). The x-axis of Fig. 4 denotes the various growth stops from this sequence and from left to right are 1) after the growth of the InGaN QW at 700 °C (labeled QW), 2) after the AlGaN IL (labeled IL + QW), 3) after annealing the AlGaN IL + InGaN QW to 850 °C (labeled 850 °C), and finally 4) after the growth of a thin GaN cap layer at 850 °C (labeled GaN). The annealing of the AlGaN IL capped InGaN QW has a profound impact on the QW emission intensity which dramatically increases and the FWHM which decreases signaling a marked improvement in the QW radiative efficiency.

As shown in Fig. 5(a), the PL emission of the non-annealed sample ("QW+IL" in Fig. 4) shows two peaks, one near 380 nm which is from the InGaN UL and one centered around 550 nm which is due to the single InGaN QW. The PL linewidth for the QW emission is 87 nm and

the PL intensity for the InGaN UL and QW are almost equivalent. An AFM image of this non-annealed AlGaN IL film is shown in Fig. 5(b). The image shows a mounded structure with an RMS roughness of 0.48 nm. The mounds are suggestive of discrete AlGaN grains with a size around 15 to 30 nm, however since this size is close to the AFM tip radius the image is likely a convolution of the AFM tip and surface morphology. In contrast, the PL emission for the annealed sample ("850 °C" in Fig. 4) shown in Fig. 5(c) is dominated by the QW emission which is ~20 times more intense compared to the non-annealed sample shown in Fig. 5(a) and has a substantially narrower linewidth of 38 nm. The AFM image of this annealed sample is shown in Fig. 5(d) and has a substantially smoother surface morphology with an RMS roughness of 0.18 nm. The increased smoothness of the annealed InGaN QW + AlGaN IL sample suggests that the film undergoes some degree of recrystallization during the annealing step. The increased smoothness of the top AlGaN IL layer after annealing is one reason for the improved heterointerfaces observed in the STEM image shown in Fig. 2(b).

Further study of the samples with and without annealing using TRPL also indicate improvement in the radiative emission rates after annealing. Fig. 6 shows the normalized PL intensity as a function of time for both samples (solid lines). The dashed lines in Fig. 6 are simple single exponential fits to quantify the change in PL lifetime. The sample without annealing has a PL lifetime of 2.7 ns while the sample with annealing has a lifetime of 9.3 ns. For typical InGaN QWs which have significant amounts of both radiative and non-radiative recombination, the measured PL decay time is a measurement of both recombination pathways. Since the only difference between the two samples is the annealing, it is expected that the radiative recombination rate is similar for both samples and, to first order, changes observed in the PL decay time can be attributed mainly to changes in the non-radiative recombination rate. This assumption is supported by noting that the PL decay time for the annealed sample shows a decay time closer to a single exponential which is indicative of a QW more dominated by radiative recombination. Furthermore, the difference in lifetimes is more than a factor of three

and indicates that the difference in PL intensity shown in Fig. 5 cannot be due to changes in light extraction between samples or other extrinsic factors. Therefore, the TRPL data suggests there is a fundamental change in the recombination rates after annealing which reduces non-radiative recombination channels and thereby improves the overall radiative efficiency.

The choice of barrier growth temperature also influences both the extent to which the IL capped QW is annealed during growth and the resultant emission efficiency and heterointerface smoothness. To explore the impact of barrier growth temperature, MQW samples with ILs were grown with barrier temperatures ranging from 800 to 900 °C. Fig. 7(a) shows the PL wavelength (red circles, left-axis) and intensity (blue-squares, right axis) for these samples plotted versus the GaN barrier growth temperature. All samples have QWs grown at 710 ºC and $Al_zGa_{1-z}N$ ILs with $z = 0.38$ that are 1.5 nm thick. As shown in Fig. 7(a) the PL wavelength decreases as the GaN barrier temperature increases while the PL intensity increases. The decrease in the PL wavelength is due to a decrease in the indium concentration, x, in the QW as the GaN barrier temperature is increased. The increase in the PL intensity is due to the commonly observed increase in PL intensity as the indium concentration decreases, similar to the improved PL intensity for blue wavelength QWs vs. green wavelength QWs. As labeled on Fig. 7(a) x decreases from 0.205 at 800 ºC to 0.18 at 900 ºC as measured from the dynamic diffraction analysis fits of the $\omega/2\theta$ scans. This gradual decrease in the indium concentration as the GaN barrier temperature increases suggests that the annealing step produces some degree of indium diffusion and some degree of recrystallization as discussed further in Section 5.2.

To examine the heterointerface quality of the samples described in Fig. 7(a), XRD measurements of the superlattice FWHM were examined as a function of the diffraction order. This analytical approach of using the XRD peak FWHM provides an assessment of the interface roughness of InGaN/GaN MQWs as reported in Refs. [38; 39] based on a formula first derived by Pan *et al.* [40]. In Fig. 7(b) the FWHM of the XRD superlattice peaks are plotted vs. angle (diffraction order) for the same films shown in Fig. 7(a). (Note that the main GaN peak occurs at

ω = 17.27 º, and therefore the absolute diffraction order increases for higher and lower angles away from that value.) In Fig. 7(b), the peakwidths for barrier temperatures > 800 ºC are offset along the y-axis so that the data does not overlap, and quadratic fits plotted as solid lines aid in demonstrating the extent of the peakwidth change as a function of angle. The larger the change in the XRD peakwidth versus angle, the less abrupt the heterointerfaces. As shown in Fig. 7(b), larger increases in peakwidth versus angle are observed for MQWs with 800 and 900 ºC barrier temperatures, compared to the samples with 850 and 875 ºC GaN barriers. This qualitative assessment of interface quality suggests that the 850 and 875 ºC GaN barrier films have smoother InGaN/AlGaN/GaN interfaces compared to the MQW films with 800 or 900 ºC GaN barriers.

4.4 Spontaneous and piezoelectric polarization effect

In this section experimental and theoretical data are explored to understand the effect of spontaneous and piezoelectric polarization induced electric fields on the emitting wavelength and efficiency of MQWs with AlGaN ILs. This is done by varying the AlGaN IL thickness to change the polarization electric field strength on the InGaN QW and the QW growth temperature to change the indium composition in the InGaN QWs.

Fig. 8 shows the experimental and theoretical data for MQWs with different IL thicknesses at three different QW growth temperatures, where emission wavelength is plotted vs. the interlayer thickness. For this data the indium concentration and $Al_zGa_{1-z}N$ IL thickness (z = 0.38) were obtained using dynamic diffraction analysis of the ω/2θ XRD scans. At fixed AlGaN thickness, reducing the QW growth temperature increases the PL wavelength due to the increased indium composition in the QW as shown for the data in Fig. 8(a). The nominal indium compositions obtained from XRD analysis are x = 0.20 at 730 ºC, x = 0.215 at 710 ºC and x = 0.24 at 700 ºC. In addition to differences in indium concentration, the wavelength is also influenced by the IL thickness; with a larger red-shift in wavelength observed as the IL thickness is increased. Fig.

8(b) shows simulation results of the band diagram and electron and hole wavefunctions for a single $In_xGa_{1-x}N$ (x = 0.215) QW and $Al_zGa_{1-z}N$ (z = 0.4) ILs with thicknesses of 1 nm (solid lines) and 2 nm (dashed lines). The thicker AlGaN interlayer increases the polarization induced electric fields within the QW increasing the energy gradient (tilt) that further separates the electron and hole states more spatially, but coincidently brings the wavefunctions closer in energy resulting in the longer wavelengths. This is similar what is observed with increased GaN barrier thickness in standard InGaN/GaN MQWs [9]. Simulations of the PL wavelength versus the AlGaN IL thickness are plotted in Fig. 8(c) and show that as the IL thickness increases the polarization induced fields within the QWs also increase resulting in a red-shift in wavelength. For these simulations, indium compositions in the QW (x = 0.19, 0.215, and 0.23) were chosen to approximately match the measured wavelength and indium compositions obtained from the XRD analysis. These choices for the indium concentrations for the simulations are close to the indium concentration estimated from the dynamic diffraction fits, which are only good to $x = \pm$ 0.01. The red-shift in wavelength with increased IL thickness matches the experimental trend, implying the shift in emission wavelength at a given indium composition is caused by the IL thickness and polarization induced electric fields.

To discern how the IL thickness influences the radiative efficiency, the measured PL intensity and calculated radiative efficiency are compared. Fig. 9(a) shows the PL intensity (or P_{out} in Eqn. 3) versus IL thickness for the same samples shown in Fig. 8(a). The PL intensities for the samples are scaled to the sample grown at 730 °C with an interlayer thickness of 1 nm using an estimated η_{rad} is ~0.3 (upper left in Fig. 9(a)). When comparing samples, changes in PL intensity are equal to changes in η_{rad} (see Section 3), so this scaling of PL intensity allows for direct comparison to the theoretical data. The experiments show with increased IL thickness and a decreased growth temperature the PL intensity (η_{rad}) decreases. Fig. 9(b) shows the simulated overlap versus interlayer thickness for the three different QW indium compositions (x = 0.19, 0.215, and 0.23). The changes in overlap indicate a change in radiative recombination

rate (see Eqn. 1). Although the decrease in overlap (R_{rad}) with IL thickness has a similar trend compared to the PL intensity shown in Fig. 8(a), the trend of indium composition and growth temperature does not exactly match. Therefore, polarization induced electric fields are not the only variable influencing the PL intensity with IL thickness.

Since an exact match of experimental PL intensity and simulated overlap is not found, Eqn. 2 suggests there is not only a radiative recombination rate change with growth temperature, but also a change in the non-radiative recombination rate. Fig. 9(c) shows the calculated radiative efficiency versus IL thickness using the overlap from Fig. 9(b), and a non-radiative recombination rate. The non-radiative recombination rate is held constant for each different IL thickness, but is different for the three different indium compositions. The non-radiative recombination rates increase with increasing In composition, and are ~5 and ~10 times higher for the QWs with x = 0.215 (710 °C) and x = 0.23 (700°C) indium compositions, respectively compared to the QWs with 0.19 (730 °C) indium composition. Therefore, a single non-radiative rate for a given indium composition produces a fit to the experimental trend with IL thickness given in Fig. 9(a). This suggests that the density of non-radiative recombination centers within the QW is not influenced by the IL thickness, but is solely influenced by the growth temperature and resulting indium composition.

5. Discussion

Here we discuss the impact of AlGaN ILs on InGaN QWs to produce longer wavelengths emission specifically: (1) how indium incorporation is increased, (2) how the QW annealing improves the interface quality and improves the emission intensity, and (3) how the increased spontaneous and piezoelectric polarization produced by the AlGaN IL red-shifts the emission wavelength.

5.1 Higher indium incorporation

In Sections 4.1 and 4.2 it was shown that AlGaN ILs enable increased indium composition in the InGaN QWs resulting in longer wavelength emission. Typically during InGaN growth, the indium coverage on the (0001) GaN surface is limited to ~ 22 % of a monolayer due to indium site blocking further adsorption [41]. Higher indium coverages of ~26% can be obtained if the temperature is lowered below 730 °C [41]. Also limiting indium incorporation is the InGaN QW coherency strain to the underlying GaN lattice [42-44] so that indium incorporation into the $In_xGa_{1-x}N$ QW is limited to x ~0.20 [11] and x ~0.22 [45]. Indium incorporation above this level requires InGaN strain relaxation [42-44] which is unlikely for the InGaN QWs in this paper since the QWs are well under the critical thickness [44; 46]. Furthermore, there no evidence of strain relaxation or dislocation generation in the STEM images shown in Fig. 2.

However, a slight and quantifiable increase in the indium concentrations up to $x = 0.24$ (as shown in Figs. 3(c) and 3(d)) is observed when the QW is capped with the AlGaN IL. For these higher indium concentrations, the QW growth temperature is 700 °C, which is consistent with the higher indium surface coverage ($x \sim 0.26$) observed at lower temperature by Jiang *et al.* [41]. Since the AlGaN IL is grown at the same temperature as the QW, it is possible that residual surface indium is incorporated into the InGaN QW and in the first few monolayers of the AlGaN IL. Evidence of a thin AlInGaN layer is observed in EDX measurements (not shown) at the InGaN/AlGaN interface, however the exact alloy concentration is difficult to discern due to the thinness of the layer. From the EDX measurements there is no indium segregation throughout or on top of the AlGaN IL. This suggests that the AlGaN IL helps the QW capture a higher indium concentration which is then uniformly distributed throughout the entire InGaN QW.

5.2 Interface smoothing and defect elimination by annealing

The AlGaN/InGaN annealing step prior to the GaN barrier growth has three consequences including; increasing the PL emission intensity as shown in Fig. 4, smoothing the AlGaN/GaN

interface as shown in Fig 5, and increasing the PL lifetime as shown in Fig. 6. All of these consequences coincide with the restructuring at the InGaN/AlGaN interface shown in the AFM images in Fig. 5. The presence of non-radiative centers is likely a consequence of the low QW growth temperature and their concentration increases as the QW growth temperature decreases as modeled in Fig. 9(c). The non-radiative centers could be impurities such as hydrogen or carbon [13] or more likely point defects [47; 48] formed to partly alleviate lattice strain. Hydrogen present from the incomplete dissociation of the metalorganics is known to be highly diffusivity in GaN [49; 50] and might desorb after diffusing through the InGaN/AlGaN layers. The concentration of these non-radiative centers is not expected to be large since $\omega/2\theta$ XRD scans with and without annealing of the single QW films shown in Fig. 4 no significant differences; however the impact of removing these point defects on PL emission intensity is tremendous. Similar impact on PL emission intensity has been demonstrated in InGaN thermal decomposition studies, where a marked decrease in the PL intensity is observed well before any structural changes are observed by XRD [37].

Also notable is the change in the top AlGaN surface layer after annealing as shown by the change from Fig. 5(b) to Fig. 5(d). The as-grown AlGaN IL shown in Fig. 5(b) has a mounded morphology which might be expected for a low temperature grown AlGaN film [12]. The observation that the AlGaN smoothens after annealing as shown in Fig. 5(d) is puzzling as the 850 ºC temperature is too low to cause significant AlGaN decomposition and metal atom reincorporation of the IL.

Instead, the AlGaN surface smoothing might be the result of strain relaxing from defect removal and a intermixing of indium and aluminum near the InGaN/AlGaN interface. Assuming that the AlGaN IL places further compressive strain on the InGaN QW compared to GaN, the roughening observed in Fig. 5(b) may be a manifestation of this added compressive strain. After annealing the surface of the AlGaN IL becomes smooth, with no indication of cracking in the AlGaN layer [51]. Recent work by Ahl and coworkers shows that the surface roughness

decreases and the indium incorporation increases as the aluminum concentration is increased in AlInGaN films [52]. Ahl and coworkers inferred that the decrease in surface roughness arises from a change in the growth mode from step flow to two dimensional, while the increase in indium incorporation compensates the increased tensile strain from the higher aluminum fraction in the AlInGaN [52]. In the present annealing situation shown in Fig. 5, no active growth occurs, however annealing the AlGaN/InGaN layers could produces some degree of strain relief, through atomic mixing near the AlGaN/InGaN interface (observed in the EDX scans), a slight loss of indium from the QW depending on the annealing temperature, and removal of non-radiative point defects. Considering the overall InGaN/AlGaN/GaN structure, a greater degree of strain balancing to GaN lattice might be expected for the InGaN QW with the AlGaN IL compared to a QW structure without the IL. However the structure change occurs after the AlGaN IL is annealed and not as the result of an overall strain balancing from all the layers.

Finally, the AlGaN IL can be thought of as a protective layer to prevent decomposition of the InGaN QW during the annealing step. Evidence of this thermal protection is observed in the EDX atomic distributions which show little evidence of indium diffusion into the AlGaN layer. The degree of this protection from indium loss is annealing temperature sensitive as shown in Fig. 7(a), where the indium concentration in the InGaN QW decreases slightly as the annealing temperature is increased from 800 to 900 °C.

The main consequence of the AlGaN IL capping of the InGaN QW followed by annealing is that smooth heterointerfaces are formed above and below the QW. Having these abrupt interfaces is consistent with previous observations that more efficient QW emission is observed in uniform, random InGaN alloys with relative smooth interfaces [21; 22].

5.3 Polarization field contribution to red-shift in wavelength

In section 4.4 the effects of the polarization induced fields and the non-radiative recombination on MQWs on the InGaN QW with AlGaN ILs were identified. Fig. 8 shows how

increasing the IL thickness red-shifts the emission wavelength due to the increased polarization induced electric field on the QW. The role of polarization induced fields has been suggested in other reports [35], but the experiments and simulation presented in Figs. 8 and 9 assuredly quantify their role. For example, a MQW with an indium composition of $x = 0.215$ with 10 nm thick GaN barriers has a simulated emission wavelength of ~527 nm. From the modeling, this same QW with a 2 nm thick $Al_{0.5}GaN_{0.5}N$ IL has an emission wavelength that increases to ~552 nm representing an additional 25 nm redshift. It should be noted that this wavelength shift from a MQW with and without an IL could be slightly less, because simulations assume abrupt heterointerfaces which occur more so for MQW with ILs compared to MQWs without ILs (see Fig. 2). Additionally, carrier screening will counteract the additional redshift in the MQWs with ILs to a greater extend compared to the MQW without the ILs.

The IL increased polarization induced electric field on the InGaN QW and its resulting red-shift without increasing the indium composition is attractive to achieve green-gap wavelengths, but there is a tradeoff with the red-shifted wavelength and efficiency. As the wavelength red-shifts, the overlap and radiative recombination rate decrease compared to the non-radiative recombination rate (Fig. 9(b)), resulting in the negative slope of radiative efficiency with increasing IL thickness shown in Figs. 9(a) and 9(c). Of course, reducing this non-radiative recombination rate will reduce this downward trend. For example, if the non-radiative rate were negligible the radiative efficiency would be 1 for any interlayer thickness as shown in Eqn. 2. The improvement in efficiency after annealing the IL, and with different barrier conditions show non-radiative recombination centers can be decreased by annealing to some degree (Figs 4-6).

A red-shift in emission wavelength can also be achieved by lowering the QW growth temperature as is done with traditional InGaN/GaN MQWs, but this too occurs at the detriment of the radiative efficiency (as suggested in Fig 1(a)) and ultimately causes the green gap. Clearly, from this work, growing or annealing the InGaN QWs at higher temperatures, as the IL

enables, improves radiative efficiency and may prove to be a more desirable pathway to higher efficiencies at longer wavelengths.

6. Conclusion

In this paper InGaN/AlGaN/GaN-based multiple quantum wells (MQWs) with AlGaN interlayers (ILs) are investigated to examine the fundamental mechanisms behind their increased radiative efficiency at wavelengths of 530 - 590 nm. The interlayer MQWs are formed by growing InGaN QWs at temperatures lower than those typically used for green wavelength QWs, growing the AlGaN IL at the QW growth temperature, annealing the AlGaN IL capped InGaN QW up to the GaN barrier growth temperature, and then growing a GaN barrier layer at elevated temperature. From the data presented, the AlGaN IL allows for increased indium incorporation into the InGaN QW and annealing the AlGaN IL is essential to produce sharp heterointerfaces and remove non-radiative recombination centers in the as grown QW. Finally, the AlGaN IL also increases the polarization induced electric fields in the InGaN QW, producing an additional red-shift in the emission wavelengths. This additional polarization induced field, in conjunction with the increased indium concentration in the QW, allows MQWs and LEDs to be produced out to red wavelengths [26].

While substantially longer wavelength QWs can be produced using AlGaN IL as presented here and initially in the Toshiba work [23-26], dramatic further improvements must occur before these green to red LEDs have the performance necessary for commercial applications. Although more indium can be captured in the AlGaN IL capped QWs, the as-grown InGaN material contains too many defects to be fully removed by annealing. The implication for conventional green wavelength emitters is that the InGaN contains too many non-radiative defects and many of the growth improvements that lessen their influence can only partially cure this problem. If these defects are generated as a result of the low temperature needed for InGaN growth or as a

means to partly relieve the InGaN strain, fully eliminating their impact will be paramount to solving the lack of bright green to red InGaN-based emitters.

Acknowledgements

J. M. Kempisty is thanked for technical assistance and K.C. Cross for AFM measurements. The single-QW annealing work was supported by the Sandia's Solid-State Lighting Science Energy Frontier Research Center, funded by the US Department of Energy, Office of Basic Energy Sciences and the MQWs growth and characterization was supported by the LDRD program at Sandia National Laboratories. Sandia National Laboratories is a multi-program laboratory managed and operated by Sandia Corporation, a wholly owned subsidiary of Lockheed Martin Company, for the U.S. Department of Energy's National Nuclear Security Administration under contract DE-AC04-94AL85000.

References

[1] Y. Narukawa, M. Ichikawa, D. Sanga, M. Sano, T. Mukai, Journal of Physics D-Applied Physics 43 (2010) 354002.

[2] M.R. Krames, O.B. Shchekin, R. Mueller-Mach, G.O. Mueller, L. Zhou, G. Harbers, M.G. Craford, Journal of Display Technology 3 (2007) 160-175.

[3] S. Lutgen, D. Dini, I. Pietzonka, S. Tautz, and A Briedennassel, A. Lell, et al., Proc. of SPIE 7953, Novel in-Plane Semiconductor Lasers X 7953 (2011) 79530G.

[4] E. Okahisa, S. Masui, T. Yanamoto, S. Nagahama, Review of Laser Engineering 41 (2013) 230-3.

[5] S. Nakamura, N. Senoh, N. Iwasa, S.I. Nagahama, Japanese Journal of Applied Physics Part 2-Letters 34 (1995) L797-L799.

[6] J.M. Phillips, M.E. Coltrin, M.H. Crawford, A.J. Fischer, M.R. Krames, R. Mueller-Mach, et al., Laser & Photonics Reviews 1 (2007) 307-333.

[7] T. Matsuoka, H. Okamoto, M. Nakao, H. Harima, E. Kurimoto, Applied Physics Letters 81 (2002) 1246-1248.

[8] R. Dahal, J. Li, K. Aryal, J.Y. Lin, H.X. Jiang, Applied Physics Letters 97 (2010) 073115.

[9] J.J. Wierer, D.D. Koleske, S.R. Lee, Applied Physics Letters 100 (2012) 111119.

[10] F. Scholz, A. Sohmer, J. Off, V. Syganow, A. Dornen, J.S. Im, A. Hangleiter, H. Lakner, Materials Science and Engineering B-Solid State Materials for Advanced Technology 50 (1997) 238-244.

[11] D.D. Koleske, S.R. Lee, G. Thaler, M.H. Crawford, M.E. Coltrin, K.C. Cross, Applied Physics Letters 97 (2010) 071901.

[12] D.D. Koleske, S.R. Lee, M.H. Crawford, K.C. Cross, M.E. Coltrin, J.M. Kempisty, Journal of Crystal Growth 391 (2014) 85-96.

[13] D.D. Koleske, A.E. Wickenden, R.L. Henry, M.E. Twigg, Journal of Crystal Growth 242 (2002) 55-69.

[14] N. Okada, K. Tadatomo, K. Yamane, H. Mangyo, Y. Kobayashi, H. Ono, K. Ikenaga, Y. Yano, K. Matsumoto, Japanese Journal of Applied Physics 53 (2014) 081001.

[15] A.M. Armstrong, M.H. Crawford, D.D. Koleske, Applied Physics Express 7 (2014) 032101.

[16] X.H. Wu, C.R. Elsass, A. Abare, M. Mack, S. Keller, P.M. Petroff, S.P. DenBaars, J.S. Speck, S.J. Rosner, Applied Physics Letters 72 (1998) 692-694.

[17] D. Cherns, Journal of Physics-Condensed Matter 12 (2000) 10205-10212.

[18] H. Yamada, K. Iso, M. Saito, H. Hirasawa, N. Fellows, H. Masui, K. Fujito, J.S. Speck, S.P. DenBaars, S. Nakamura, Physica Status Solidi-Rapid Research Letters 2 (2008) 89-91.

[19] V. Fiorentini, F. Bernardini, F. Della Sala, A. Di Carlo, P. Lugli, Physical Review B 60 (1999) 8849-8858.

[20] I.H. Ho, G.B. Stringfellow, Applied Physics Letters 69 (1996) 2701-2703.

[21] C. Wetzel, T. Salagaj, T. Detchprohm, P. Li, J.S. Nelson, Applied Physics Letters 85 (2004) 866-868.

[22] M.J. Galtrey, R.A. Oliver, M.J. Kappers, C.J. Humphreys, P.H. Clifton, D. Larson, D.W. Saxey, A. Cerezo, Journal of Applied Physics 104 (2008) 013524.

[23] R. Hashimoto, J. Hwang, S. Saito, S. Nunoue, in: H. Yamaguchi, K. Kumakura (Eds.), Physica Status Solidi C: Current Topics in Solid State Physics, Vol 10, No 11, 2013, pp. 1529-1532.

[24] S. Saito, R. Hashimoto, J. Hwang, S. Nunoue, Applied Physics Express 6 (2013) 111004.

[25] R. Hashimoto, J. Hwang, S. Saito, S. Nunoue, physica status solidi (c) 11 (2014) 628-631.

[26] J.-I. Hwang, R. Hashimoto, S. Saito, S. Nunoue, Applied Physics Express 7 (2014) 071003.

[27] Y.-D. Lin, S. Yamamoto, C.-Y. Huang, C.-L. Hsiung, F. Wu, K. Fujito, H. Ohta, J.S. Speck, S.P. DenBaars, S. Nakamura, Applied Physics Express 3 (2010) 082001.

[28] J.R. Creighton, W.G. Breiland, D.D. Koleske, G. Thaler, M.H. Crawford, Journal of Crystal Growth 310 (2008) 1062.

[29] S. Nakamura, Japanese Journal of Applied Physics Part 2-Letters 30 (1991) L1705.

[30] S.R. Lee, A.M. West, A.A. Allerman, K.E. Waldrip, D.M. Follstaedt, P.P. Provencio, D.D. Koleske, C.R. Abernathy, Applied Physics Letters 86 (2005) 241904.

[31] D.D. Koleske, J.J. Wierer, Jr., A.J. Fischer, S.R. Lee, Journal of Crystal Growth 390 (2014) 38-45.

[32] S.R. Lee, D.D. Koleske, M.H. Crawford, J.J. Wierer, Journal of Crystal Growth 355 (2012) 63.

[33] The NEXTNANO3 software package can be downloaded from www.nextnano.de.

[34] I. Vurgaftman, J.R. Meyer, L.R. Ram-Mohan, Journal of Applied Physics 89 (2001) 5815-5875.

[35] T. Shioda, H. Yoshida, K. Tachibana, N. Sugiyama, S. Nunoue, Physica Status Solidi a-Applications and Materials Science 209 (2012) 473-476.

[36] D.M. Graham, A. Soltani-Vala, P. Dawson, M.J. Godfrey, T.M. Smeeton, J.S. Barnard, M.J. Kappers, C.J. Humphreys, E.J. Thrush, Journal of Applied Physics 97 (2005) 103508.

[37] G.T. Thaler, D.D. Koleske, S.R. Lee, K.H.A. Bogart, M.H. Crawford, Journal of Crystal Growth 312 (2010) 1817.

[38] Y.H. Kwon, G.H. Gainer, S. Bidnyk, Y.H. Cho, J.J. Song, M. Hansen, S.P. DenBaars, Applied Physics Letters 75 (1999) 2545-2547.

[39] J.C. Zhang, et al., Applied Physics Letters 87 (2005) 071908.

[40] Z. Pan, Y.T. Wang, Y. Zhuang, Y.W. Lin, Z.Q. Zhou, L.H. Li, R.H. Wu, Q.M. Wang, Applied Physics Letters 75 (1999) 223-225.

[41] F. Jiang, R.-V. Wang, A. Munkholm, S.K. Streiffer, G.B. Stephenson, P.H. Fuoss, K. Latifi, C. Thompson, Applied Physics Letters 89 (2006) 161915.

[42] Z. Liliental-Weber, M. Benamara, J. Washburn, J.Z. Domagala, J. Bak-Misiuk, E.L. Piner, J.C. Roberts, S.M. Bedair, Journal of Electronic Materials 30 (2001) 439-444.

[43] S. Pereira, M.R. Correia, E. Pereira, K.P. O'Donnell, E. Alves, A.D. Sequeira, N. Franco, I.M. Watson, C.J. Deatcher, Applied Physics Letters 80 (2002) 3913-3915.

[44] M. Leyer, J. Stellmach, C. Meissner, M. Pristovsek, M. Kneissl, Journal of Crystal Growth 310 (2008) 4913-4915.

[45] T.M. Smeeton, C.J. Humphreys, J.S. Barnard, M.J. Kappers, Journal of Materials Science 41 (2006) 2729-2737.

[46] D. Holec, Y. Zhang, D.V.S. Rao, M.J. Kappers, C. McAleese, C.J. Humphreys, Journal of Applied Physics 104 (2008) 123514.

[47] A. Uedono, T. Tsutsui, T. Watanabe, S. Kimura, Y. Zhang, M. Lozacaposh, et al., Journal of Applied Physics 113 (2013) 123502.

[48] A. Uedono, S. Ishibashi, N. Oshima, R. Suzuki, Japanese Journal of Applied Physics 52 (2013) 08JJ02.

[49] C.H. Seager, S.M. Myers, A.F. Wright, D.D. Koleske, A.A. Allerman, Journal of Applied Physics 92 (2002) 7246-7252.

[50] K. Orita, M. Meneghini, H. Ohno, N. Trivellin, N. Ikedo, S. Takigawa, M. Yuri, T. Tanaka, E. Zanoni, G. Meneghesso, Quantum Electronics, IEEE Journal of 48 (2012) 1169-1176.

[51] S.R. Lee, D.D. Koleske, K.C. Cross, J.A. Floro, K.E. Waldrip, A.T. Wise, S. Mahajan, Applied Physics Letters 85 (2004) 6164-6166.

[52] J.P. Ahl, J. Hertkorn, H. Koch, B. Galler, B. Michel, M. Binder, B. Hollaender, Journal of Crystal Growth 398 (2014) 33-39.

Figure Captions

Fig. 1. (a) PL scans of MQWs with AlGaN ILs grown at three different QW growth temperatures along with microscope images of the surface under PL excitation. (b) PL intensity versus wavelength (left axis) for MQWs with AlGaN ILs (red circles) and without AlGaN ILs (blue squares). PL FWHM versus wavelength (right axis) for MQWs with AlGaN ILs (green diamonds). The solid lines are power law fits for the intensity vs. wavelength plot and a guide for the eyes for the FWHM versus wavelength.

Fig. 2. STEM images of 5 period MQWs (a) with the InGaN QWs grown at 730 ºC and the GaN barriers grown at 800 ºC, and (b) with the QWs capped with AlGaN ILs at 700 ºC and the GaN barriers grown at 850 ºC. The inset for each image shows the atomically resolved planes for a single MQW period.

Fig. 3. X-ray diffraction $\omega/2\theta$ scans of MQW with and without AlGaN IL. For the samples shown in (a) and (b), the QWs are grown at (a) 725 °C and (a) 730 °C, without an AlGaN IL, and a GaN barrier grown at 800 °C. Also the QW in (b) is grown 4 times faster than (a). For the samples shown in (c) and (d), the QWs were grown at 700 °C, capped with the AlGaN IL, followed by ramping the growth temperature to either (c) 800 °C or (d) 850 °C for the growth of the GaN barrier layer.

Fig. 4. PL intensity (left side) and peak width (right side) of a single InGaN QW with an AlGaN IL growth sequence. The QW is grown at 700 °C (first point), followed by the AlGaN IL at 700 °C (second point), followed by heating the QW and AlGaN IL to 850 °C (third point), and finally after a thin GaN cap layer grown at 850 °C (fourth point).

Fig. 5. PL Intensity (a) and AFM scans (b) of the single InGaN QW and AlGaN IL after growth at 700 °C. PL Intensity (c) and AFM scans (d) of the single InGaN QW and AlGaN IL after

annealing at 850 °C. The PL scans were measured using a HeCd 325 nm cw laser at a power of 1.1 mW. The AFM scan size is 500 nm x 500 nm.

Fig. 6. Time-resolved PL data measured for the samples with (red solid line) and without (blue solid line) the 850 °C anneal. The dashed lines are single exponential fits.

Fig. 7. Influence of the GaN barrier growth temperature on the luminescence and structural properties for InGaN QW grown at 710 °C capped with a 1.5 nm thick $Al_{0.38}Ga_{0.62}N$ IL. In (a) the PL wavelength (red-left) and intensity (blue-right) are plotted vs. the GaN barrier growth temperature. In (b) the XRD linewidths were measured from a $\omega/2\theta$ scan and are plotted vs. ω for each of the different GaN barrier growth temperatures. The XRD peak width is offset by the amount denoted along the right of the data for clearer viewing, and a quadratic fit is shown for each set of barrier growth temperatures. The up and down arrows denote the angle of the (0002) reflection of the main GaN peak.

Fig. 8. Experimental wavelength versus AlGaN IL thickness (a) for QW growth temperatures of 700, 710 and 730 ºC, showing the increase in wavelength as the QW growth temperature decreases and the AlGaN IL thickness increases. Simulation results of the band diagram and electron and hole wavefunctions (b) for a single $In_xGa_{1-x}N$ (x = 0.215) QW and $Al_zGa_{1-z}N$ (z = 0.4) ILs with thicknesses of 1 nm (solid lines) and 2 nm (dashed lines). Simulation results of wavelength versus AlGaN IL thickness (c) for three different $In_xGa_{1-x}N$ QW indium compositions (x), listed in the Figure.

Fig. 9. Experimental PL intensity (a), modeled electron and hole wavefunction overlap squared (b), and modeled radiative efficiency (c) plotted versus the AlGaN IL thickness, for the samples shown in Fig. 8. In (a) a decrease in the PL intensity is observed as the QW growth temperature

decreases, and as the AlGaN IL thickness increases. In (b) the modeled overlap squared is modeled for the three indium compositions determined in Fig 8. In (c) the radiative efficiency is calculated using the radiative recombination rate used in (b) along with an increasing nonradiative rate as the indium composition increases. Nonradiative rates are ~5 and ~10 times higher in the x = 0.215 and 0.23 $In_xGa_{1-x}N$ QWs, respectively compared to $In_xGa_{1-x}N$ QW with x = 0.19.

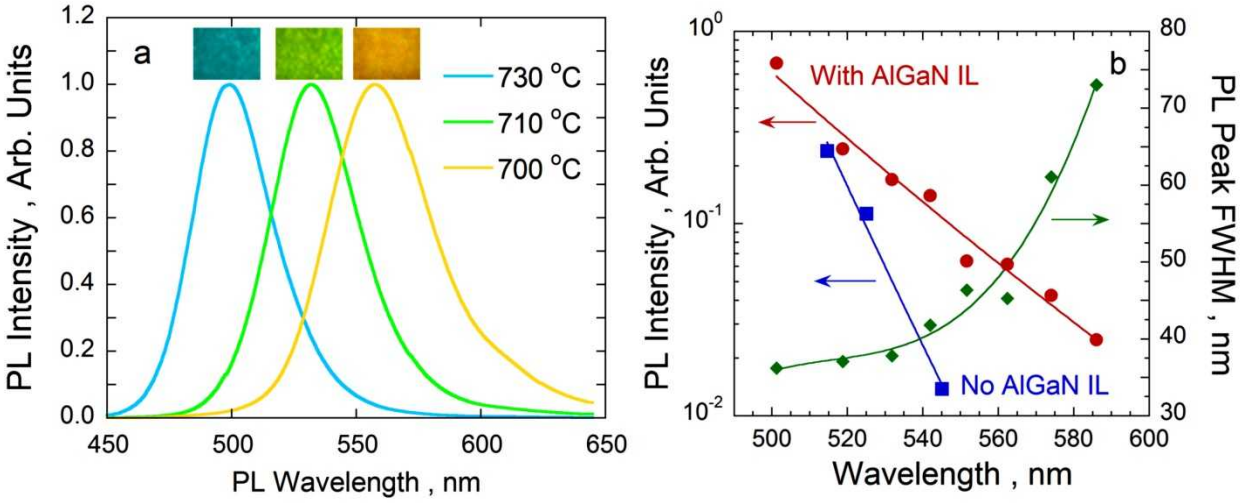
a
730 °C
710 °C
700 °C
PL Intensity , Arb. Units
PL Wavelength , nm
b
With AlGaN IL
No AlGaN IL
PL Intensity , Arb. Units
PL Peak FWHM , nm
Wavelength , nm

Fig. 1.

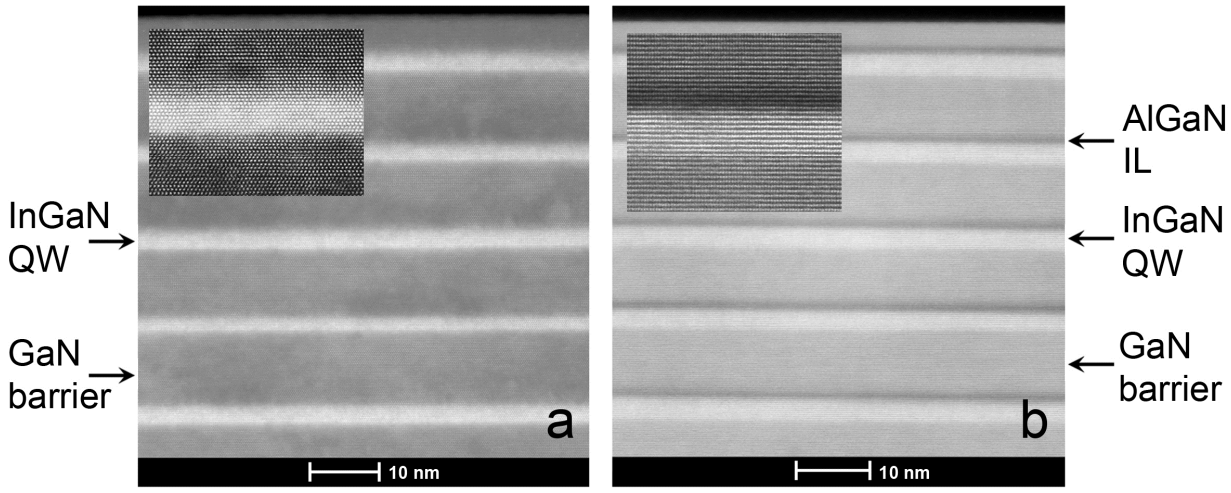
InGaN
QW
GaN
barrier
a
10 nm
AlGaN
IL
InGaN
QW
GaN
barrier
b
10 nm

Fig. 2.

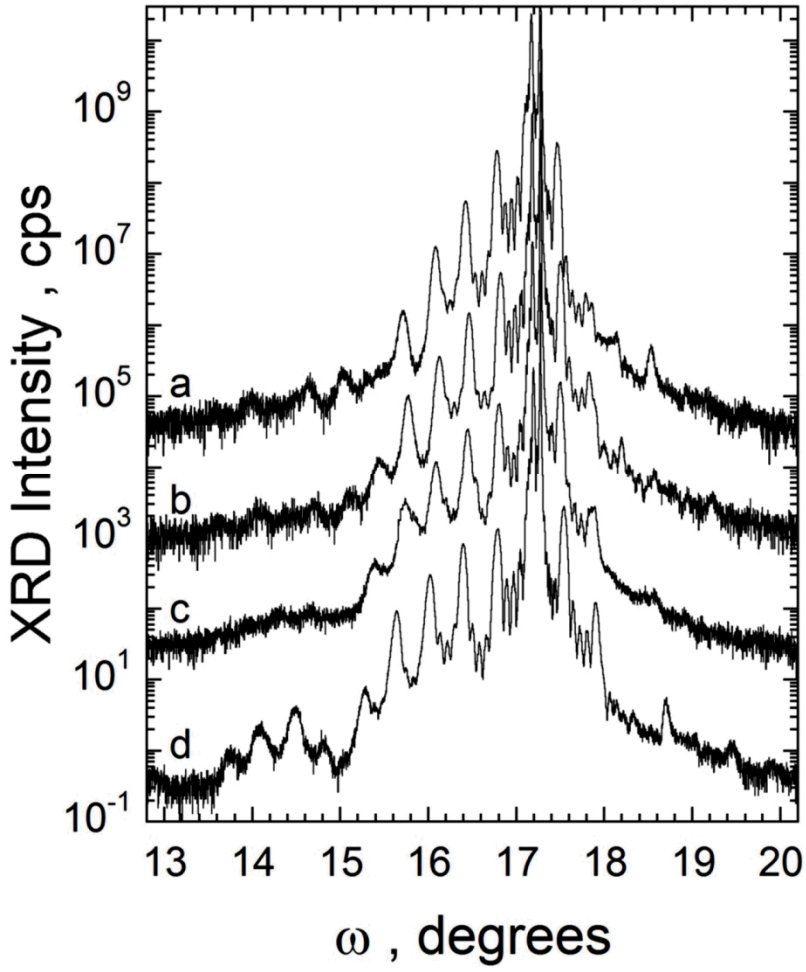
XRD Intensity , cps
10^9
10^7
10^5
10^3
10^1
10^{-1}
a
b
c
d
13
14
15
16
17
18
19
20
ω , degrees

Fig. 3.

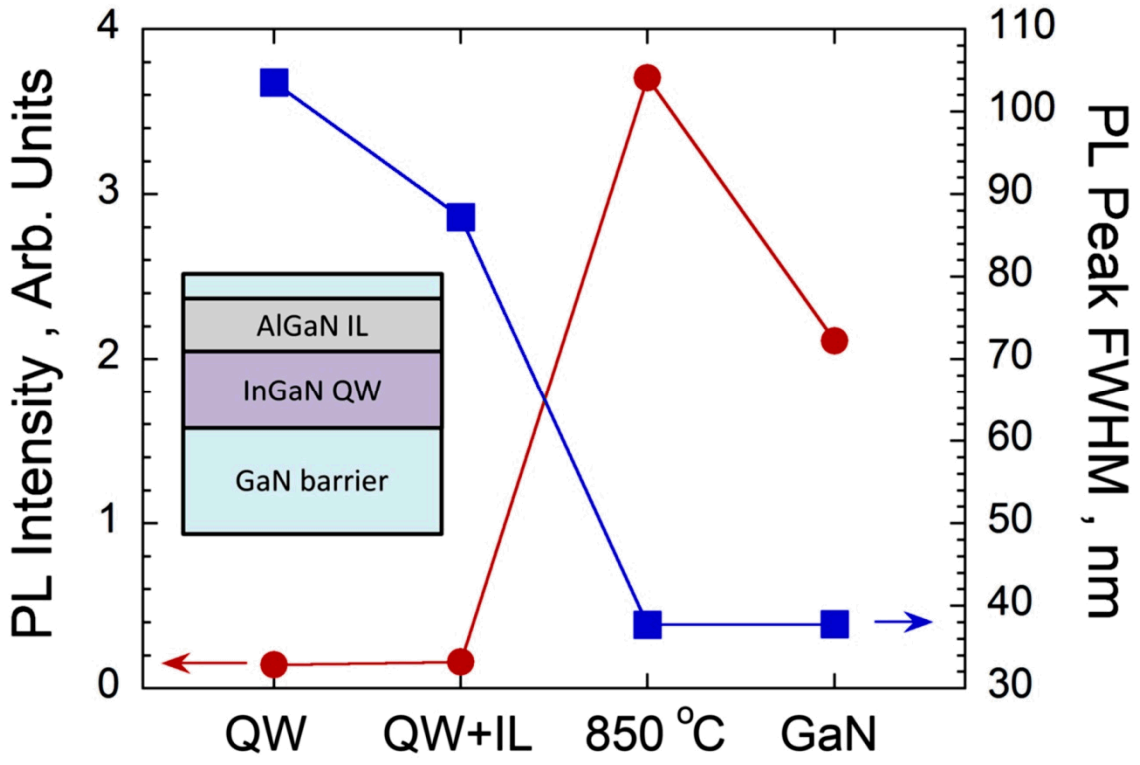
PL Intensity , Arb. Units
PL Peak FWHM , nm
AlGaN IL
InGaN QW
GaN barrier
QW
QW+IL
850 °C
GaN
0
1
2
3
4
30
40
50
60
70
80
90
100
110

Fig. 4.

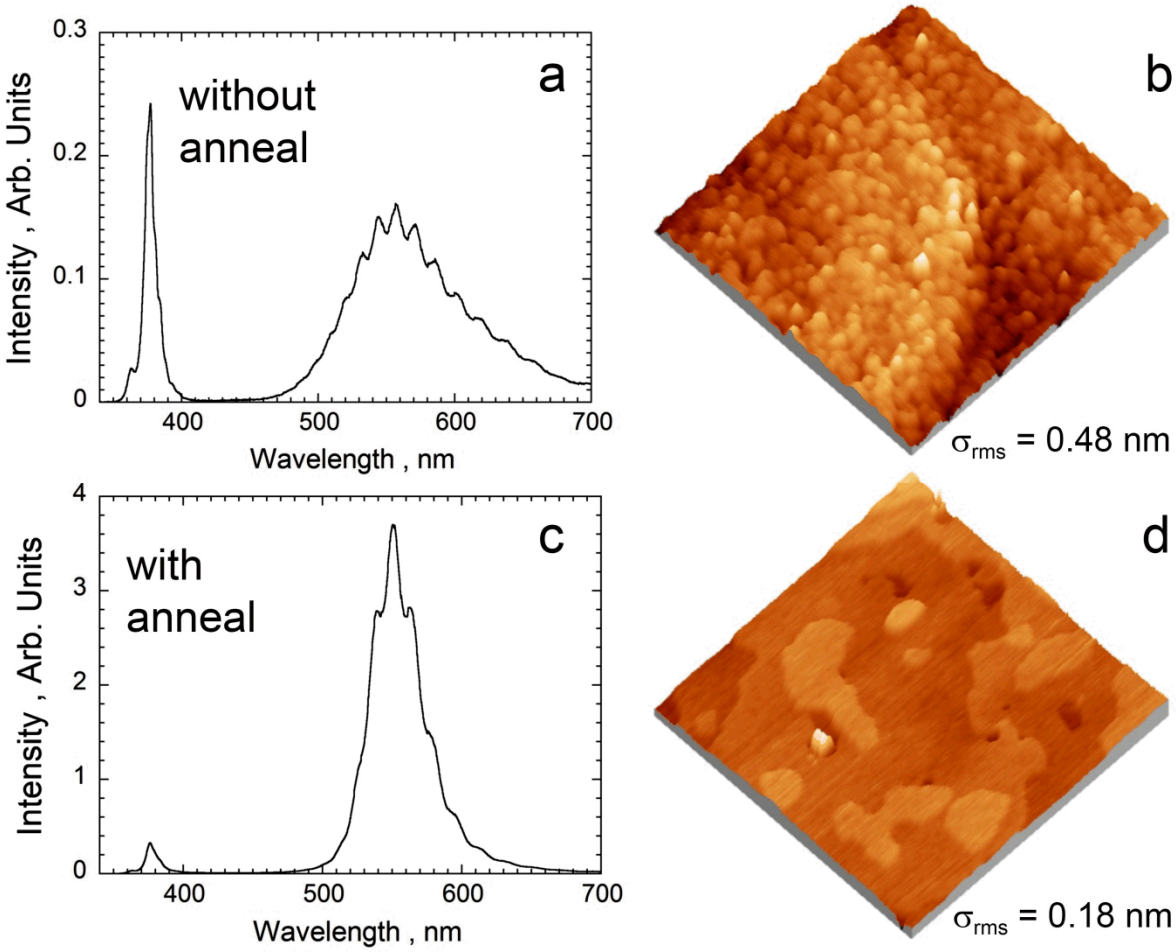
a
without
anneal
Intensity , Arb. Units
Wavelength , nm
b
σrms = 0.48 nm
c
with
anneal
Intensity , Arb. Units
Wavelength , nm
d
σrms = 0.18 nm

Fig. 5.

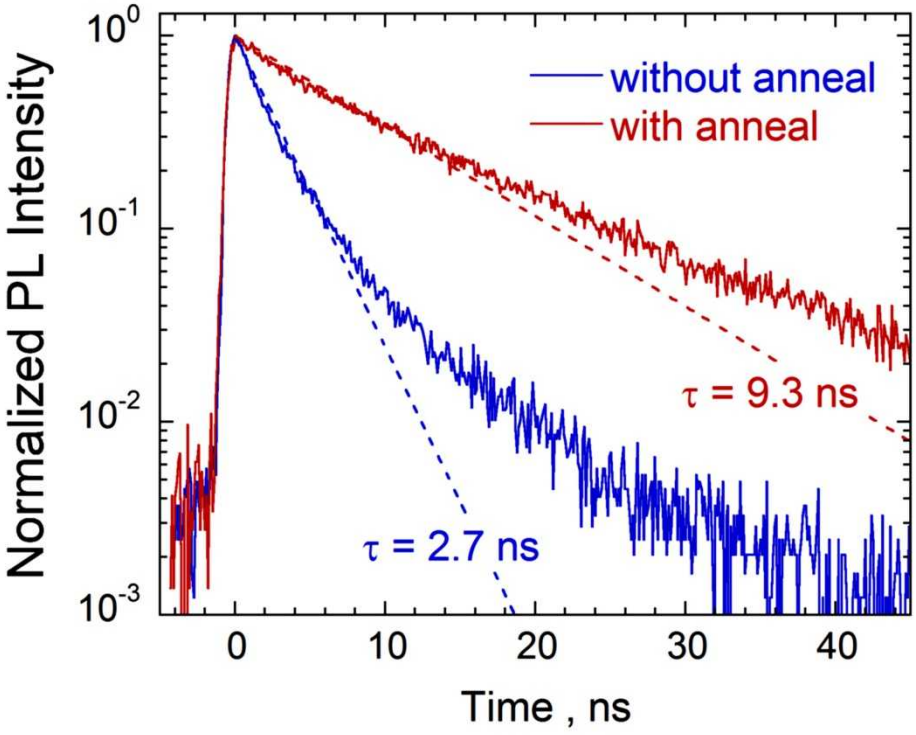
Normalized PL Intensity
10^0
10^{-1}
10^{-2}
10^{-3}
0
10
20
30
40
Time , ns
without anneal
with anneal
τ = 9.3 ns
τ = 2.7 ns

Fig. 6.

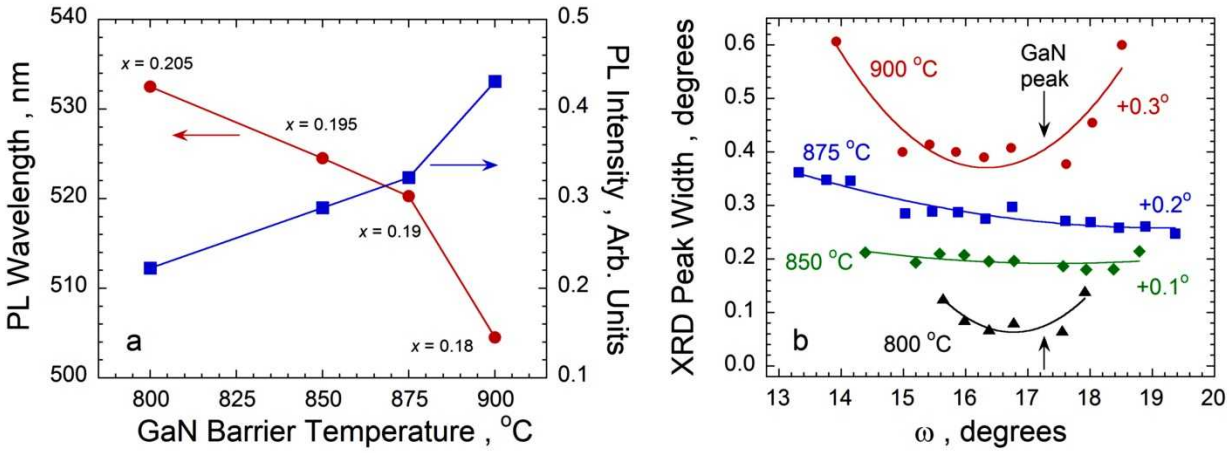
PL Wavelength , nm
PL Intensity , Arb. Units
GaN Barrier Temperature , °C
x = 0.205
x = 0.195
x = 0.19
x = 0.18
a
XRD Peak Width , degrees
ω , degrees
900 °C
GaN peak
+0.3°
875 °C
+0.2°
850 °C
+0.1°
800 °C
b

Fig. 7.

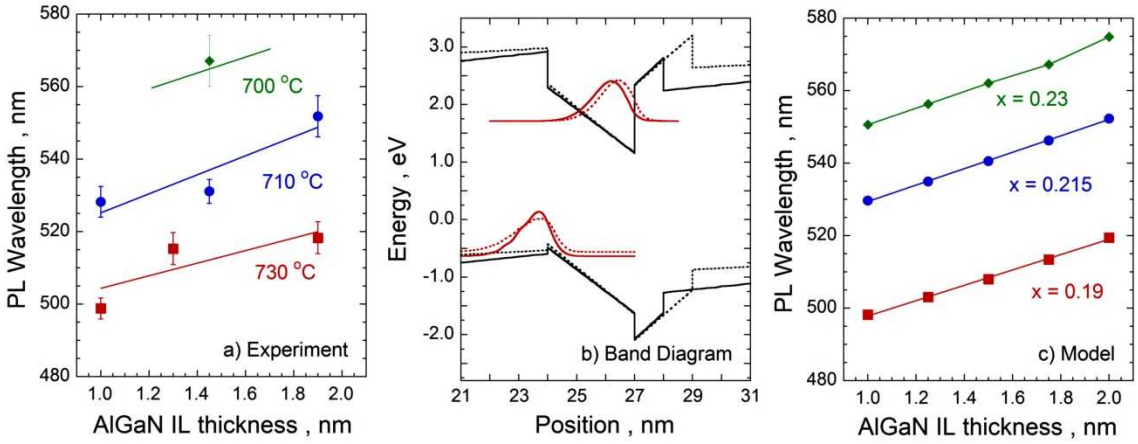
PL Wavelength , nm
AlGaN IL thickness , nm
700 °C
710 °C
730 °C
a) Experiment
Energy , eV
Position , nm
b) Band Diagram
PL Wavelength , nm
AlGaN IL thickness , nm
x = 0.23
x = 0.215
x = 0.19
c) Model

Fig. 8.

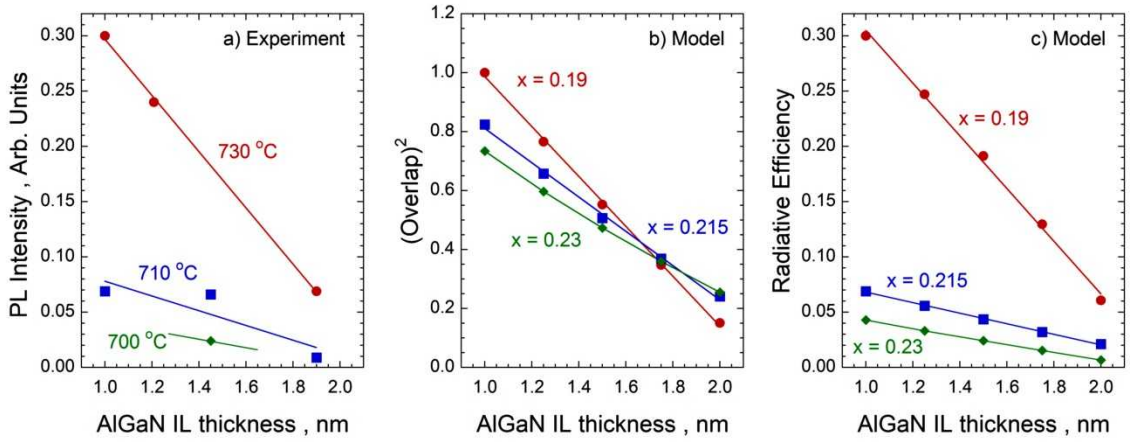
a) Experiment
PL Intensity , Arb. Units
730 °C
710 °C
700 °C
AlGaN IL thickness , nm
b) Model
(Overlap)^2
x = 0.19
x = 0.215
x = 0.23
AlGaN IL thickness , nm
c) Model
Radiative Efficiency
x = 0.19
x = 0.215
x = 0.23
AlGaN IL thickness , nm

Fig. 9.